Optica Applicata, Vol. LV, No. 4, 2025
DOI: 10.37190/oa/204502

Highly sensitive gamma-ray radiation dosimeter utilizing one-dimensional ternary annular porous photonic crystal comprising polymer-doped dye integration

Ayman A. Ameen[1], Suneet Kumar Awasthi[2,*], Nassir Saad Alarifi[3], Mostafa R. Abukhadra[4], Jacob Wekalao[5], Wail Al Zoubi[6], Hussein A. Elsayed[7], Ahmed Mehaney[7,*]

[1] Physics Department, Faculty of Science, Sohag University, Egypt

[2] Department of Physics and Material Science and Engineering, Jaypee Institute of Information Technology, Noida 201304, U.P., India

[3] Geology and Geophysics Department, College of Science King Saud University, Riyadh, Saudi Arabia

[4] Geosciences Department, College of Science, United Arab Emirates University, 15551, Al Ain, United Arab Emirates

[5] Department of Optics and Optical Engineering, University of Science and Technology of China, Hefei 230026, China

[6] Materials Electrochemistry Laboratory, School of Materials Science and Engineering, Yeungnam University, Gyeongsan 38541, Republic of Korea

[7] Photonic and phononic crystals Lab., Physics Department, Faculty of Science, Beni-Suef University, Beni-Suef 62512, Egypt

[*]Corresponding author: ahmed011236@science.bsu.edu.eg

This research introduces a photonic sensor designed to detect gamma-ray radiation, utilizing a one-dimensional regular ternary annular photonic crystal (1D APhC) structure. The sensor consists of alternating layers of porous silicon, silicon dioxide, and polyvinyl alcohol (PVA) polymer, which is doped with crystal violet and carbol fuchsine dyes. Exposure to varying levels of gamma-ray radiation alters the refractive index of the doped polymer, resulting in a shift in the photonic band-gap (PBG). The analysis of this dosimeter emphasizes how the intensity and position of the left band edge of the PBG are affected. Theoretical investigations are performed using Bruggeman's effective medium equation and the transfer matrix method (TMM). The study examines the impact of gamma-ray radiation intensity, ranging from 0 to 70 Gy, on the refractive index of the polymer. Furthermore, it explores how critical parameters, such as the movement of the left and right band edges, PBG width, and sensor sensitivity, are influenced by structural modifications. Under optimized conditions, the sensor achieves a sensitivity of 200.8351 nm/RIU in detecting gamma-ray radiation exposure from 0 to 70 Gy. This highly sensitive dosimeter design holds significant potential for various scientific applications, facilitating accurate detection of gamma-ray radiation.

Keywords: annular photonic crystal, polymer, doped dye integration, gamma radiation, dosimeter.

1. Introduction

Hybrid organic-inorganic optical materials are emerging as a key focus in modern technological advancements due to their unique combination of properties derived from both inorganic and polymeric components [1-5]. Hybrid nanocomposites (NCs) effectively integrate the mechanical, electrical, and optical characteristics of inorganic materials with the flexibility and processability of polymer matrices. Among these polymers, polyvinyl alcohol (PVA) has gained substantial industrial significance due to its environmentally friendly, non-toxic nature and superior thermal, chemical, and optical stability. Similarly, carboxymethyl cellulose (CMC), a water-soluble, semi-crystalline polymer, is widely recognized for its low cost, non-toxic attributes, and extensive industrial applications [5-7]. When combined in a 50/50 ratio, PVA and CMC exhibit enhanced dielectric properties, reduced absorption edge, and improved thermal stability, making them highly suitable for advanced material applications.

Nanocomposites incorporating PVA/CMC/ZnS-NiO demonstrate promising potential for γ-ray radiation dose detection, particularly within the range of 0 to 75 kGy [1-8]. The process of γ-ray irradiation is widely employed to modify polymer structures through mechanisms such as grafting, degradation, and crosslinking. Upon exposure to γ-radiation, polymer chains undergo a series of chain reactions, leading to the formation of chemically active free radicals. These radicals initiate structural alterations, promote the formation of new bonds, and facilitate chain crosslinking, ultimately modifying the material's physical and chemical properties [8-10]. Additionally, γ-ray irradiation often induces visible color changes in polymers, providing a crucial visual indicator of structural modifications. Such changes enhance the applicability of these materials in radiation sensing and dosimetry [9-15].

Photonic crystals (PhCs) are periodic composite structures where the interfaces between adjacent dielectric layers function as weak scattering centers. Depending on the structural arrangement of these layers, PhCs can be categorized as one-dimensional (1D), two-dimensional (2D), or three-dimensional (3D) structures. One of the defining characteristics of PhCs is the formation of photonic bandgaps (PBGs), which are frequency regions where light propagation is restricted due to variations in the refractive indices of the constituent materials [16-25]. Disruptions in the periodicity of PhCs can lead to photon localization, a critical phenomenon in the development of photonic crystal -based sensors. For example, DAHER *et al*. introduces a highly sensitive biosensor based on a one-dimensional binary photonic crystal made of germanium and titanium nitride layers. A defect layer placed in the center of the structure is used to identify cells affected by diabetes by detecting changes in refractive index. The device performs especially well under transverse electric (TE) polarization, with a peak sensitivity of 2676.66 nm/RIU. Its design is not only effective but also simple and cost-efficient, making it suitable for real-time biomedical diagnostics [26]. Another research work of DAHER *et al*. presented a novel biosensor designed with a ternary photonic crystal structure using layers of silicon, titanium nitride, and silicon dioxide. The sensor targets the detection

of creatinine levels in blood serum, a key indicator of kidney function. Utilizing a central defect cavity, the device detects slight changes in refractive index linked to creatinine concentration. The sensor achieves a high sensitivity of up to 938.02 nm/RIU, especially under TE polarization, and is noted for its practicality, affordability, and real-time monitoring capabilities [27]. An ultrasensitive binary photonic sensor design composed of Si/TiN layers for detection of blood sugar concentration was proposed by DAHER. His design achieved exceptional high sensitivity of 4200 nm/RIU [28]. DAHER *et al*. also presents a binary photonic crystal sensor for detecting the chikungunya virus in blood samples like plasma and platelets. They have optimized Si/TiN-based multilayer structure loaded with platelets and plasma samples separately yielding the high sensitivity of 2306 nm/RIU and 2833, respectively. The sensor's effectiveness can be further increased with both angle of incidence and cavity thickness [29]. Within the field of radiation detection, photonic crystal-based dosimeters have demonstrated remarkable efficiency. Porous photonic crystals (PPCs), in particular, offer superior sensing capabilities compared to conventional PhCs, owing to their larger surface area and tunable pore sizes, which enhance interaction with radiation-exposed materials [25,30-34].

Porous silicon (PSi), a silicon wafer with a network of nanopores, is widely utilized in photonic structures for its unique optical properties. In the proposed dosimeter design, alternating layers of porous silicon are employed, with the pores filled with polyvinyl alcohol (PVA) polymer doped with crystal violet (CV) and carbol-fuchsine (CF) dyes. The embedded polymer is subjected to γ-ray radiation exposure from a Co-radioactive source within a dosage range of 0–70 Gy [10-15]. The primary objective of this research is to evaluate the effectiveness of the proposed structure in radiation detection by analyzing the shift in the resonance wavelength at the left band edge of the PBG. Furthermore, the study explores the impact of key geometrical parameters—including the inner core radius, the thickness and porosity of the first layer, and the thickness of the second layer—on the sensor's performance. Through systematic optimization, the most suitable geometrical configurations are identified to achieve a highly sensitive dosimeter structure, ensuring precise radiation detection for various industrial, medical, and scientific applications.

2. Architectural details

The proposed γ-ray dosimeter design is composed of a 1D ternary annular photonic crystal which comprises alternating layers of layers of porous silicon, silicon dioxide and polyvinyl alcohol (PVA) polymer doped with crystal violet and carbol-fuchsine dyes. The porous of silicon (PSi) and SiO_2 are infiltrated with PVA polymer doped with integrated CV and CF dyes [13,35-38]. The structural design of the proposed dosimeter whose tri-layer unit cell is repeated N times and represented by the equation $[\text{layer A}/\text{layer B}/\text{layer C}]^N$ is shown in Fig. 1.

The structure consists of 30 repeating periods ($N = 30$), ensuring an optimized PBG for efficient radiation detection. The key geometric parameters are carefully selected

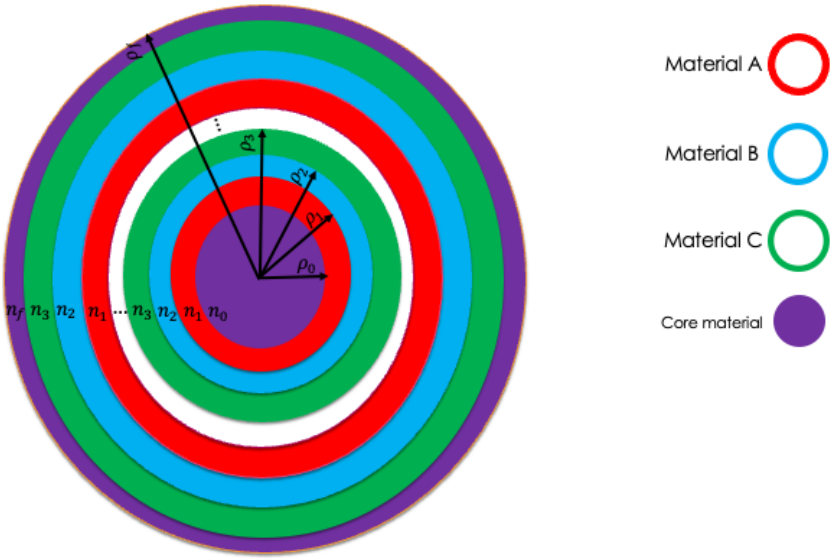

Fig. 1. Schematic representation of the proposed dosimeter design consisting of a 1D ternary annular photonic crystal [layer A/layer B/layer C]^N. The red, blue and green rings are representing PSi, SiO_2 and PVA polymer doped with integrated CV and CF dye materials of the design. The purple color solid disk and rings are indicating core and outer cylindrical layer of the dosimeter. The notations n_i and ρ_i represent the refractive index and radius of the i-th cylindrical layer of the design, respectively. Here i = 0, 1, 2, 3 and f denotes the core, first, second, third and substrate cylindrical layers of the design, respectively.

to enhance the sensor's performance. The first layer (A) of the structure has a porosity of 0.7 and a thickness of 50 nm, while the second layer (B) has a porosity of 0.7 and thickness of 60 nm. The thickness of the third layer (C) of PVA polymer doped with (CV + CF) is 25 nm.

The inner core and outer cylindrical layers of the dosimeter are composed of silicon dioxide (SiO_2) of refractive index of 1.45. The inner core radius of cylindrical layer of the designed is chosen to 500 nm for ensuring effective light confinement and interaction within the structure. Additionally, the refractive index of silicon is considered 3.7, which plays a crucial role in the optical response of the annular photonic crystal sensor. This structural design enables precise control over the interaction between electromagnetic waves and γ-ray-exposed materials, making the proposed dosimeter highly sensitive and suitable for various scientific, industrial, and medical applications. The proposed 1D TPhC can be easily fabricated via a layer-by-layer deposition technique on a cylindrical silica core as discussed below.

PSi layer formation: Created by electrochemical anodization of heavily doped p-type silicon wafers in a solution of HF and ethanol (*e.g.*, 1:1 ratio) under controlled current density to achieve ~50 nm thickness and desired porosity (*e.g.*, 0.7).

SiO_2 layer deposition: Applied using plasma-enhanced chemical vapor deposition (PECVD) or sol-gel spin coating, adjusted to ~60 nm thickness.

PVA polymer layer (dye doping): Crystal violet (CV) and carbol-fuchsine (CF) dyes are dissolved in a 10% w/v aqueous PVA solution, stirred at 60°C until homogenous. The mixture is drop-cast or spin-coated onto the SiO_2 layer to a ~25 nm thickness.

Repetition ($N = 30$): The repetitive 1D array of these tri-layers of period 30, under low-temperature deposition methods to avoid thermal degradation of dyes can be fabricated.

3. Theoretical formulation

To analyze the propagation of electromagnetic waves within the proposed annular photonic sensor, a comprehensive theoretical framework is developed. The core and cladding regions of the sensor are defined by their respective radial distances, denoted as ρ_0 (core radius) and ρ_f (cladding radius) from the sensor's axis of symmetry. The determination of radius ρ_i of any i-th cylindrical layer, which has a thickness of d_i, is based on its position within the periodic structure, considering the alternating arrangement of odd and even layers. The mathematical expression governing the radial distances of these layers is formulated as follows [39-42].

$$\rho_i = \begin{cases} \rho_0 + \dfrac{i-1}{2}\Delta + d_{\mathrm{a}} \\ \rho_0 + \dfrac{i}{2}\Delta \end{cases} \tag{1}$$

Here, $\Delta = d_{\mathrm{a}} + d_{\mathrm{b}} + d_{\mathrm{c}}$ represents the periodicity of the sensor. The notation d_{a}, d_{b} and d_{c} are used to represent thicknesses of layers A, B and C of the structure, respectively. It is assumed that cylindrical electromagnetic waves (EMWs) propagate radially outward from the core of the structure, starting at $\rho_0 = 0$. The governing equation for a cylindrical wave in the case of s-polarized light can be expressed as follows [39-42].

$$\rho \frac{\partial}{\partial \rho}\left(\rho \frac{\partial E_z}{\partial \rho}\right) - \rho^2 \frac{1}{\mu}\frac{\partial \mu}{\partial \rho}\frac{\partial E_z}{\partial \rho} + \frac{\partial}{\partial \varphi}\left(\frac{\partial E_z}{\partial \varphi}\right) + \omega^2 \mu \varepsilon \rho^2 E_z = 0 \tag{2}$$

As the z-axis is considered the axis of symmetry, the solution for the electric field in Eq. (2) depends solely on the radial distance r and the azimuthal angle φ and is expressed as follows:

$$E_z(\rho, \varphi) = V(\rho)\Phi(\varphi) = \left[CJ_m(k\rho) + DY_m(k\rho)\right]\exp(im\rho) \tag{3}$$

In this solution, J_m and Y_m denote the Bessel and Neumann functions, respectively, corresponding to the azimuthal mode number m. The propagation constant for cylindrical electromagnetic waves (EMWs) within a material of permittivity ε and permeability μ is given by $k = \omega(\mu\varepsilon)^{1/2}$. To derive the azimuthal component of the magnetic field H_φ, Maxwell's curl equation has been utilized.

$$\nabla \times E = -j\omega\mu H \tag{4}$$

$$H_{\varphi}(\rho, \varphi) = U(\rho)\Phi(\varphi) = -ip\left[CJ'_m(k\rho) + DY'_m(k\rho)\right]\exp(im\rho) \tag{5}$$

In Eq. (5), the symbols J'_m and Y'_m denote the first-order derivatives of the Bessel and Neumann functions, respectively. Subsequently, the transfer matrix is derived to relate the electric and magnetic fields at the interfaces r_{i-1} and r_i within the *i*-th layer of refractive index n_i of the sensor, as outlined in references [39-42].

$$\begin{bmatrix} V(\rho_i) \\ U(\rho_i) \end{bmatrix} = M_i \begin{bmatrix} V(\rho_{i-1}) \\ U(\rho_{i-1}) \end{bmatrix} = \begin{bmatrix} M_i(1,1) M_i(1,2) \\ M_i(2,1) M_i(2,2) \end{bmatrix} \begin{bmatrix} V(\rho_{i-1}) \\ U(\rho_{i-1}) \end{bmatrix} \tag{6}$$

The elements of the transfer matrix M_i for the *i*-th layer of the sensor are provided as follows:

$$M_i(1,1) = \frac{\pi}{2} k_i \rho_{i-1}\left[Y'_m(k_i\rho_{i-1}) J_m(k_i\rho_i) - J'_m(k_i\rho_{i-1}) Y_m(k_i\rho_i)\right] \tag{7}$$

$$M_i(1,2) = j\frac{\pi}{2}\frac{k_i}{p_i}\rho_{i-1}\left[J_m(k_i\rho_{i-1}) Y_m(k_i\rho_i) - Y_m(k_i\rho_{i-1}) J_m(k_i\rho_i)\right] \tag{8}$$

$$M_i(2,1) = -j\frac{\pi}{2} k_i \rho_{i-1} p_i\left[Y'_m(k_i\rho_{i-1}) J'_m(k_i\rho_i) - J'_m(k_i\rho_{i-1}) Y'_m(k_i\rho_i)\right] \tag{9}$$

$$M_i(2,2) = \frac{\pi}{2} k_i \rho_{i-1}\left[J_m(k_i\rho_{i-1}) Y'_m(k_i\rho_i) - Y_m(k_i\rho_{i-1}) J'_m(k_i\rho_i)\right] \tag{10}$$

where J_m, Y_m, J'_m, and Y'_m refer to the Bessel and Neumann functions, along with their first-order derivatives, respectively, for the azimuthal number *mmm*. The propagation constant and the admittance of the *i*-th cylindrical layer of the structure are given by $k_i = \omega\sqrt{\varepsilon_i \mu_i}$ and $p_i = \omega\sqrt{\varepsilon_i/\mu_i}$, respectively. The overall transfer matrix *Z*, which represents the entire structure $[\text{layer A} / \text{layer B} / \text{layer C}]^N$, can be derived as follows:

$$Z = Z_1 Z_2 \ldots Z_N = \begin{bmatrix} Z_{11} & Z_{12} \\ Z_{21} & Z_{22} \end{bmatrix} \tag{11}$$

The following equation can be applied to compute the transmission coefficient of the proposed sensor:

$$t = \frac{4}{\pi\rho_0 H^1_{\mathrm{m}}(k_0\rho_0) H^2_{\mathrm{m}}(k_0\rho_0)} \frac{1}{(jp_0 S^{(1)}_{m0} Z - Z_{21}) - jp_f S^{(2)}_{mf}(-jp_0 S^{(1)}_{m0} Z_{12} - Z_{22})} \tag{12}$$

The elements Z_{11}, Z_{12}, Z_{21}, and Z_{22} represent the components of the 2×2 transfer matrix for the entire structure. The symbols p_i and p_f denote the admittances of the core and substrate, respectively. Finally, the transmittance of the entire annular photonic sensor can be determined as described in references [39-42].

$$T = tt^* = |t|^2 \tag{13}$$

The performance of the proposed γ-ray radiation dosimeter is assessed by determining the sensitivity of the sensor, which is calculated using the transmittance of the sensor design from Eqs. (1) to (13). Mathematically, the sensitivity is defined as:

$$S = \frac{\delta\lambda}{\delta n} \tag{14}$$

Here, $\delta\lambda$ represents the shift in the left band edge of the PBG of the sensor, resulting from the corresponding change in the refractive index of the sample δn being examined.

3.1. Refractive index of the porous silicon (PSi) layer

To evaluate the performance of the proposed sensor, the following equations are utilized to calculate the refractive index of layer A made up of PSi whose pores are filled with PVA polymer doped with CV and CF dyes as referenced in [43-48]

$$n_{\mathrm{PSi}} = \frac{1}{2}\sqrt{\chi + \varphi} \tag{15}$$

In Eq. (15), the symbols χ and φ are defined as follows:

$$\chi = 3P(n_{\mathrm{PVA}}^2 - n_{\mathrm{Si}}^2) + (2n_{\mathrm{Si}}^2 - n_{\mathrm{PVA}}^2) \tag{16}$$

and

$$\varphi = \sqrt{\chi^2 + 64\, n_{\mathrm{PVA}}^2 n_{\mathrm{Si}}^2} \tag{17}$$

In this work, n_{Si} and n_{PVA} represent the refractive indices of silicon and polymer materials, respectively. The refractive index of silicon (n_{Si}) is considered to be 3.7.

3.2. Refractive index of doped polymer

The solvent casting method is employed for the preparation of PVA polymer doped with CV and CF dyes. These films are exposed to γ-ray radiation at room temperature, with dosage strengths D_γ ranging from 0 Gy (unexposed) to 70 Gy. The radiation source is assumed to be a cobalt-60 (^{60}Co) radioactive isotope.

The refractive index n_{PVA} of the PVA-doped (CV + CF) polymer is dependent on both the wavelength λ and γ-ray radiation dosage (D_γ), as expressed in the following equation [43-48]:

$$n_{\mathrm{PVA}} = P\lambda^3 + Q\lambda^2 + R\lambda + S \tag{18}$$

To derive Eq. (18), cubic curve fitting is applied to the experimental data of PVA-doped (CV + CF) using MATLAB. The refractive index n_{PVA} is calculated at $\lambda = 555$ nm. The values of the constants P, Q, R, and S, which vary with γ-ray radiation dosage, are presented in Table 1.

T a b l e 1. Values of the constants for PVA-doped (CV + CF) under different γ-ray radiation exposure levels.

D_γ	$P \times 10^{-7}$	Q	R	S
0	1.7479	−0.00025167	0.11796	−15.571
10	1.5689	−0.00022845	0.1083	−14.282
20	1.3002	−0.00019042	0.090693	−11.606
30	1.2167	−0.00017806	0.084739	−10.663
40	1.0444	−0.00015298	0.07293	−8.87
50	1.013	−0.00014864	0.070913	−8.5343
60	0.9754	−0.00014305	0.068283	−8.1388
70	0.96042	−0.00014056	0.067049	−7.9382

4. Result and discussions

First the index of refraction of first layer A of porous silicon of porosity 0.7 of width 50 nm dependent on the γ-ray radiation is examined. The pores of the layer A are infiltrated with PVA polymer doped with CV and CF dyes which are exposed with γ-ray radiation doses of strength 0 to 70 Gy. Figure 2 illustrates the refractive index

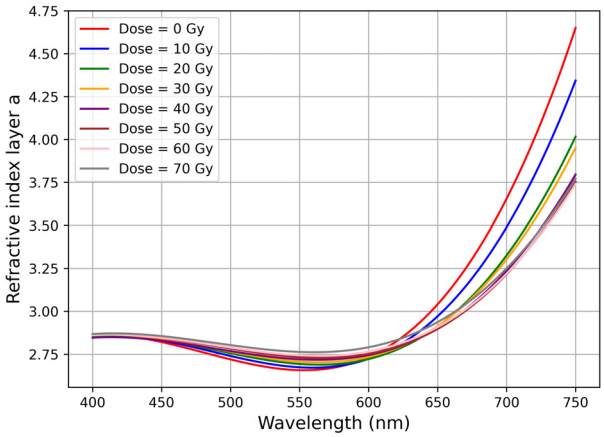

Fig. 2. Variation of the refractive index of layer A with wavelength for different gamma-ray radiation doses (0–70 Gy). The graph demonstrates how exposure to gamma radiation alters the refractive index, with higher doses leading to a gradual reduction, especially at longer wavelengths. The stability in the mid-wavelength range (450–600 nm) ensures reliable optical sensing, making the material suitable for gamma-ray dosimetry applications.

variation of layer A as a function of wavelength under different γ-ray radiation doses (0–70 Gy). The refractive index remains relatively stable in the mid-wavelength range (450–600 nm) but exhibits a dip around 550 nm before increasing sharply at higher wavelengths (above 650 nm). Notably, lower radiation doses (0 and 10 Gy) result in a higher refractive index, whereas higher doses (50 Gy and above) lead to a gradual reduction, indicating that gamma irradiation alters the optical properties of the polymer.

This trend suggests that increasing radiation exposure affects the structural and electronic properties of the polymer, potentially due to molecular modifications induced by gamma rays. The observed refractive index changes, especially at higher wavelengths, highlight the sensor's ability to detect radiation exposure levels effectively. The stability in the 450 to 600 nm region ensures reliable optical measurements, making this material a promising candidate for radiation dosimetry applications.

Next, index of refraction of second layer B of porous SiO_2 of porosity 0.7 of width 60 nm dependent on the γ-ray radiation is investigated. The pores of the layer B are infiltrated with PVA polymer doped with CV and CF dyes which are exposed with γ-ray radiation doses of strength 0 to 70 Gy. Figure 3 illustrates the variation of the refractive index of layer B as a function of wavelength for different radiation doses ranging from 0 to 70 Gy. The refractive index remains relatively stable in the lower wavelength range but increases significantly beyond approximately 600 nm, with higher refractive indices observed at longer wavelengths. The effect of radiation dose is evident, as the refractive index is highest for the 0 Gy condition and systematically decreases with increasing dose, particularly at higher wavelengths. This suggests that radiation exposure influences the optical properties of the material, potentially altering its transparency and light propagation characteristics.

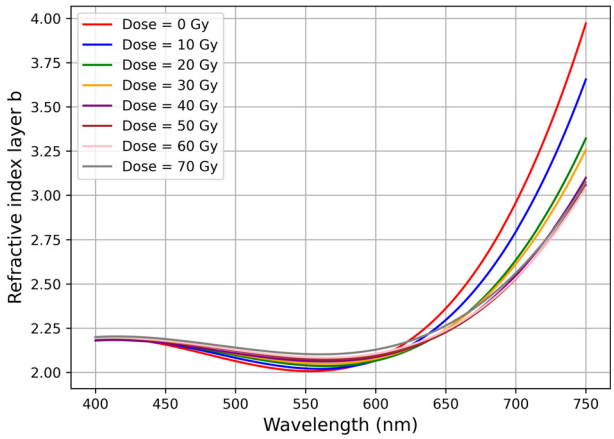

Fig. 3. Variation of the refractive index of layer B as a function of wavelength for different radiation doses (0 to 70 Gy). The refractive index remains relatively stable at lower wavelengths but increases significantly beyond 600 nm. Higher radiation doses result in a reduction of the refractive index, with a more pronounced effect at longer wavelengths, indicating changes in the optical properties of the material due to radiation exposure.

The distinct separation of curves at higher wavelengths indicates a more pronounced impact of radiation on the refractive index in this region. While lower doses (10 to 30 Gy) show a gradual decline in refractive index compared to the 0 Gy condition, higher doses (40 to 70 Gy) exhibit a more convergent behavior, suggesting a saturation effect in the material's optical response. This trend implies that beyond a certain radiation threshold, further exposure may not significantly alter the refractive index. Such findings are crucial for applications involving radiation-exposed optical materials, where understanding wavelength-dependent refractive index changes can help optimize material performance in environments with high radiation exposure.

Figure 4 presents the variation of the refractive index of layer C of PVA polymer doped with integrated CV and CF of thickness 25 nm as a function of wavelength for different radiation doses ranging from 0 to 70 Gy. Similar to previous observations, the refractive index remains relatively stable at lower wavelengths but increases significantly beyond 600 nm. The highest refractive index is observed for the 0 Gy condition, with a systematic decrease as the radiation dose increases. This indicates that radiation exposure alters the optical properties of layer C, particularly at longer wavelengths where the difference becomes more pronounced.

At lower wavelengths (400–600 nm), the refractive index variations among different doses are minimal, suggesting that radiation has a less significant effect in this region. However, at higher wavelengths, the refractive index decreases more noticeably with increasing radiation dose, potentially indicating material modifications due to radiation exposure. The trend suggests a saturation effect, where further increases in radiation dose beyond a certain threshold result in smaller changes in refractive index. These findings are essential for applications where precise control of optical properties under radiation exposure is required.

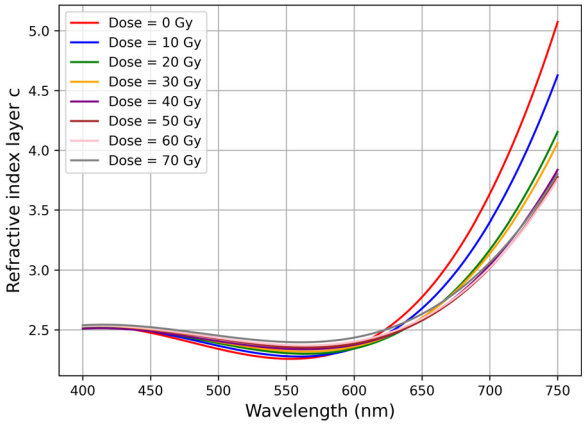

Fig. 4. Refractive index variation of layer C as a function of wavelength for different radiation doses (0 to 70 Gy). The refractive index remains nearly constant at lower wavelengths but increases significantly beyond 600 nm. Higher radiation doses lead to a gradual reduction in the refractive index, with the most noticeable changes occurring at longer wavelengths, indicating the impact of radiation on the optical properties of the material.

After investigating the dependence of the refractive indices of materials of layers A, B and C of the proposed γ-ray radiation dosimeter under the influence of different γ-ray radiation doses, efforts are given to obtain most appropriate values of the thicknesses of layers A, B and C of the structure yielding suitable PBG characteristics of the structure. First the effect of change in the thickness of layer A on the PBG properties of the structure for sensing is discussed. Table 2 presents the impact of varying the thickness of layer A on key PBG parameters, sensitivity, and intensity. As the layer thickness increases from 20 to 50 nm, the left edge and right edge of the PBG shift towards higher wavelengths, indicating a redshift in the optical response. This shift suggests that increasing the thickness of layer A leads to greater photon confinement and modifies the refractive index contrast.

T a b l e 2. Effect of layer A thickness on PBG characteristics, sensitivity, and intensity. The table presents variations in the left and right edges of the PBG, PBG width, PBG central wavelength, sensitivity, and average peak intensity as a increasing thickness of layer A, demonstrating its impact on the optical performance of the proposed sensor.

Layer A thickness [nm]	PBG left edge [nm]	PBG right edge [nm]	PBG width [nm]	Sensitivity [nm/RIU]	Average peak intensity [a.u.]	PBG center [nm]
20	458.85	506.95	48.1	151.0330491	0.999988707	482.9
22.5	467.4	518.35	50.95	155.0608339	0.999992809	492.875
25	475.75	530.25	54.5	159.8951733	0.999995246	503
27.5	484	543.2	59.2	163.461012	0.999996738	513.6
30	492.15	558.05	65.9	168.5011206	0.999997677	525.1
32.5	500.35	578.15	77.8	172.8499314	0.99999828	539.25
35	508.65	685.2	176.55	177.1206687	0.999998671	596.925
37.5	517.15	678.2	161.05	180.9853415	0.999998921	597.675
40	526	670.8	144.8	185.0094675	0.999999064	598.4
42.5	535.35	662.75	127.4	188.9131846	0.999999083	599.05
45	545.55	653.85	108.3	192.9022562	0.999998652	599.7
47.5	557.2	643.4	86.2	196.8395449	0.999994338	600.3
50	572.05	629.65	57.6	200.8351204	0.999856509	600.85

The PBG width initially expands with thickness, reaching a maximum of 176.55 nm at 35 nm, before gradually decreasing beyond this point. This trend suggests an optimal thickness for maximizing the PBG width, which is crucial for applications requiring a broad photonic response. Similarly, sensitivity increases with thickness, reaching 200.83 nm/RIU at 50 nm, making the structure highly responsive to refractive index variations. The average peak intensity remains nearly constant (~0.999999) throughout, confirming the structural stability of the photonic sensor. The PBG center wavelength shifts towards 600.85 nm at 50 nm, further demonstrating that increasing the layer thickness significantly affects the optical performance of the sensor.

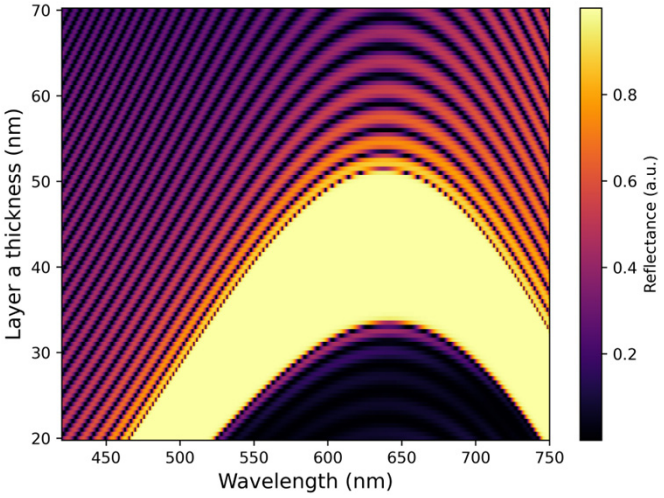

Fig. 5. Reflectance heatmap illustrating the dependence of photonic bandgap characteristics on the thickness of layer A. The color scale represents reflectance intensity, with brighter regions indicating higher reflectance. The observed redshift and broadening of the PBG with increasing layer thickness demonstrate its impact on the optical properties of the proposed structure.

Overall, the results highlight a critical trade-off between PBG width, sensitivity, and structural stability, indicating that an optimal thickness range exists for maximizing sensor performance.

Figure 5 illustrates the variation in reflectance as a function of wavelength and the thickness of layer A in the proposed photonic crystal structure. The color gradient, ranging from dark purple (low reflectance) to bright yellow (high reflectance), depicts the PBG formation and its evolution with increasing layer thickness. As the thickness of layer A increases, the PBG shifts toward longer wavelengths, indicating a redshift in the spectral response. This shift is attributed to the increase in optical path length, which affects the constructive and destructive interference of electromagnetic waves within the structure.

Additionally, the reflectance intensity distribution exhibits periodic variations, suggesting the presence of multiple resonance modes. The widening of the PBG with increasing thickness signifies enhanced light confinement and stronger photonic interactions, which are crucial for sensor sensitivity optimization. These results highlight the significant influence of layer A thickness on the optical characteristics of the structure, making it a critical parameter for tuning sensor performance.

Further efforts are dedicated to study the influence of the thickness of first layer A on sensitivity, left PBG edge, right PBG edge and PBG width as discussed below.

4.1. Effect of changing the thickness of layer A

Sensitivity *vs.* layer A thickness. Panel (a) of Fig. 6 illustrates the variation of sensor sensitivity with the thickness of layer A. The observed linear increase in sensitivity

suggests that a thicker layer enhances the sensor's ability to detect refractive index variations. This behavior can be attributed to the increased optical interaction volume within the structure, which amplifies the effective refractive index change upon analyte introduction. Consequently, optimizing layer A thickness is crucial for achieving higher sensor performance. In this case the sensitivity of the sensor reaches to maximum of 200.8351204 nm/RIU corresponding to 50 nm thickness of layer A of the structure.

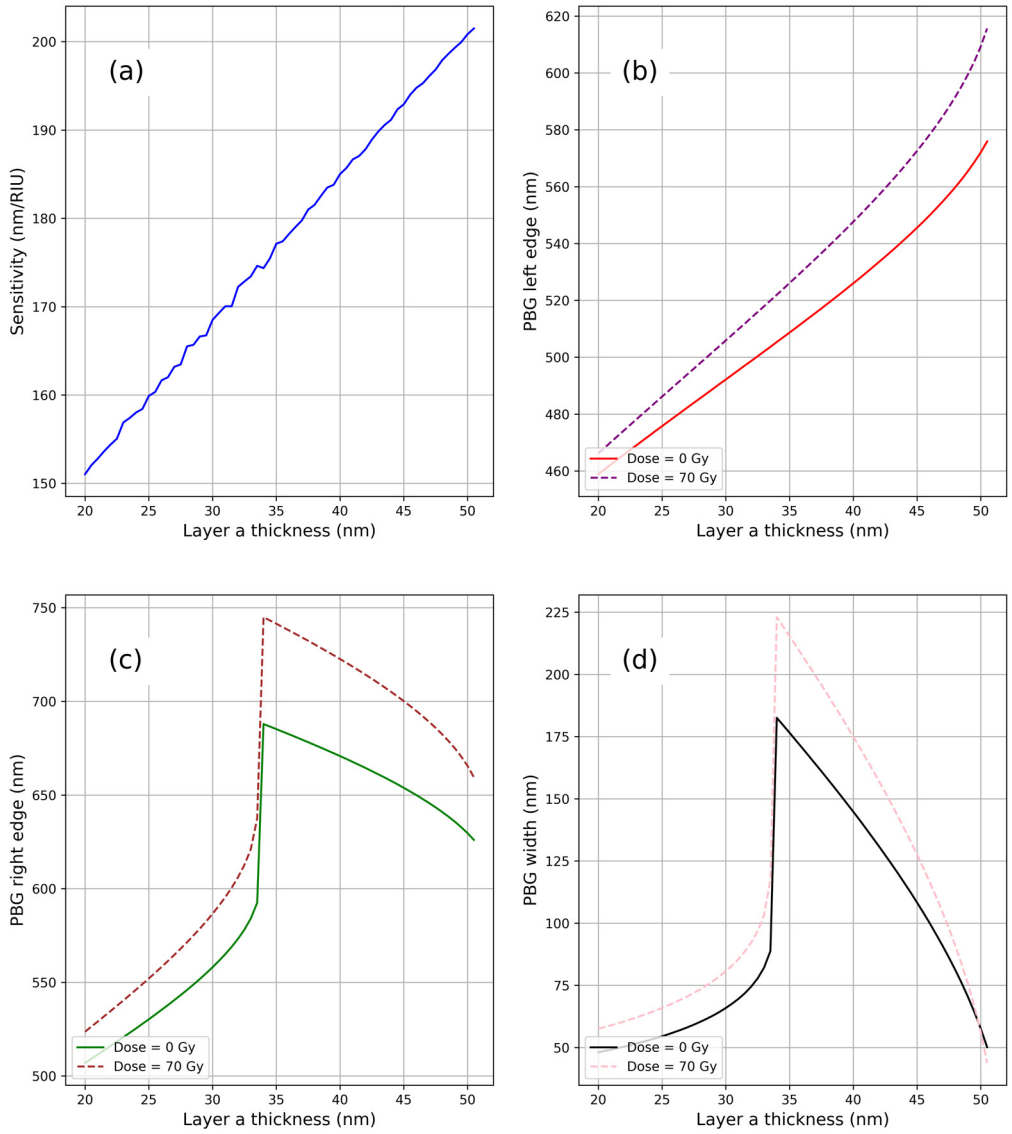

Fig. 6. Effect of layer A thickness on the optical properties of the proposed photonic structure. (a) Sensitivity variation, (b) shift in the PBG left edge, (c) shift in the PBG right edge, and (d) PBG width variation. The influence of gamma radiation exposure (0 and 70 Gy) on these parameters is also presented.

PBG width *vs.* layer A thickness. Panel (d) shows the variation in PBG width with layer A thickness under different radiation exposures. Initially, the PBG width increases with thickness, reaching a peak, followed by a decline. This trend suggests an optimal thickness range where maximum bandgap formation occurs. Beyond this range, structural dispersion effects may lead to reduced photonic confinement, thereby narrowing the PBG. The comparison between irradiated and non-irradiated cases further confirms that gamma radiation significantly modifies the photonic band characteristics, altering the optimal design parameters of the sensor.

Thus, based on above discussion the thickness of first layer A of the structure is fixed to 50 nm as it matches the high sensitivity with a wide photonic bandgap. For calculating the thickness of other layers of the structure, the thickness of layer A of the structure is fixed to 50 nm.

Further, we have investigated how the variation in the thickness of layer B influences several PBG parameters, including the left and right edges, PBG width, sensitivity, average peak intensity, and center wavelength. The data presented in Table 3 summarises the effect of change in the thickness of layer B of the structure on its PBG properties.

Figure 7 presents the reflectance variations as a function of both wavelength and the thickness of layer B. The color gradient in the plot, ranging from black to yellow, represents the reflectance intensity, with darker regions indicating lower reflectance and lighter regions corresponding to higher reflectance. A distinct interference pattern emerges, characterized by alternating bright and dark bands, which signifies construc-

T a b l e 3. Effect of layer B thickness on PBG characteristics, sensitivity, and intensity. The table presents variations in the left and right edges of the PBG, PBG width, PBG central wavelength, sensitivity, and average peak intensity as an increasing thickness of layer B, demonstrating its impact on the optical performance of the proposed sensor.

Layer B thickness [nm]	PBG left edge [nm]	PBG right edge [nm]	PBG width [nm]	Sensitivity [nm/RIU]	Average peak intensity [a.u.]	PBG center [nm]
30	483.85	542.4	58.55	165.6079	0.999994	513.125
32.5	489.95	553.25	63.3	169.2002	0.999996	521.6
35	496.1	565.95	69.85	171.9436	0.999997	531.025
37.5	502.25	583.35	81.1	174.7966	0.999998	542.8
40	508.5	685.15	176.65	177.471	0.999998	596.825
42.5	514.85	679.95	165.1	180.5069	0.999999	597.4
45	521.4	674.55	153.15	183.5218	0.999999	597.975
47.5	528.15	668.85	140.7	186.3822	0.999999	598.5
50	535.25	662.8	127.55	189.0873	0.999999	599.025
52.5	542.8	656.2	113.4	192.2725	0.999999	599.5
55	551.05	648.9	97.85	195.1605	0.999997	599.975
57.5	560.45	640.4	79.95	197.8795	0.999989	600.425
60	572.05	629.65	57.6	200.8351	0.999857	600.85

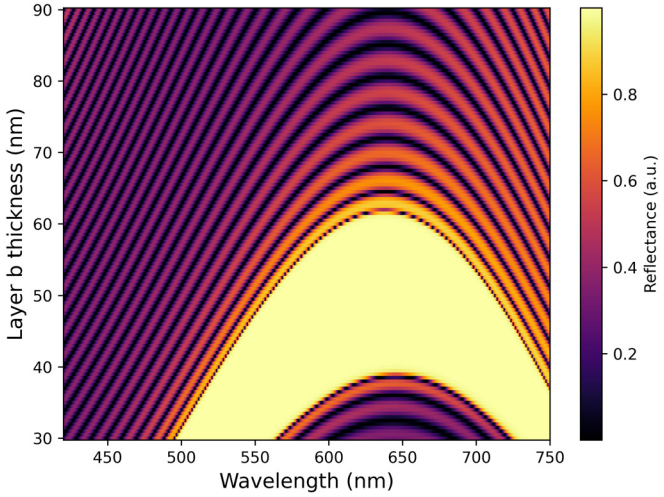

Fig. 7. Reflectance map showing the dependence of reflectance intensity on wavelength and layer B thickness. The color gradient represents reflectance values, with darker regions indicating lower reflectance and lighter regions representing higher reflectance. A distinct PBG region is observed, where light within a specific wavelength range is strongly reflected. The periodic interference pattern highlights the influence of layer thickness on optical properties, which is crucial for the design of optical coatings and sensor applications.

tive and destructive interference effects. The broad high-reflectance region in the middle of the plot suggests the formation of a PBG, where light within a specific wavelength range is strongly reflected.

As the thickness of layer B increases, the central wavelength of the high-reflectance region shifts, demonstrating the dependence of optical properties on structural parameters. The periodic nature of the reflectance bands implies a systematic modulation in the optical response of the system. This behavior is crucial for designing optical devices such as filters and sensors, where precise control over reflectance properties is essential. The figure effectively highlights how structural variations influence the reflection characteristics, making it valuable for understanding and optimizing multilayer optical coatings.

The effect of changing thickness of second layer B on sensitivity, left PBG edge, right PBG edge and PBG width of the structure is discussed here. Before discussing this impact, we have plotted the dependence of second layer thickness on the sensitivity, left PBG edge, right PBG edge and PBG width of the structure. This plot is shown in the Fig. 8 which is plotted from the data of Table 3.

4.2. Effect of changing the thickness of layer B

Sensitivity *vs.* layer B thickness. The first graph shown in Fig. 8(a) illustrates the relationship between layer B thickness and sensitivity. It demonstrates a positive linear correlation, where an increase in thickness leads to an enhancement in sensitivity. This

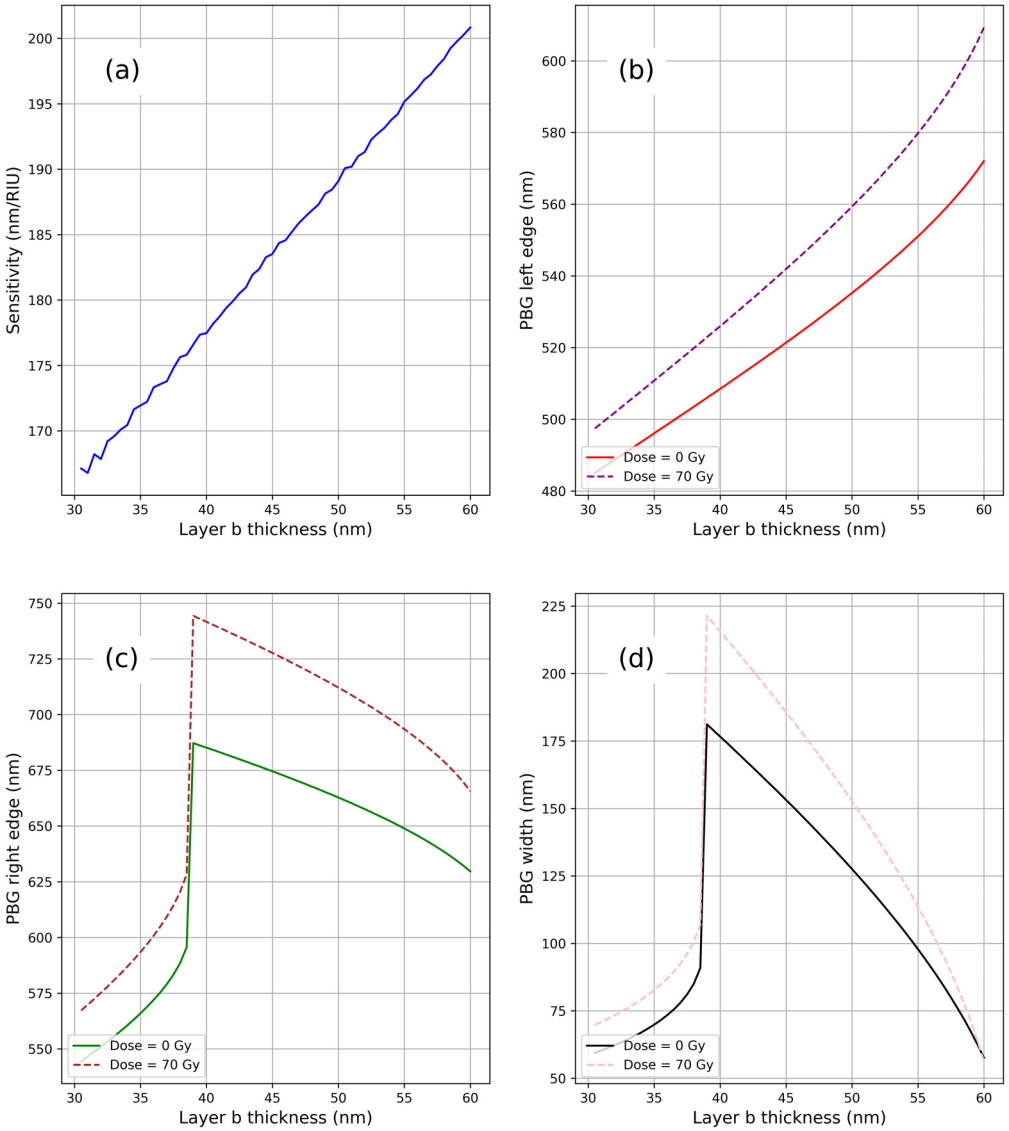

Fig. 8. Effect of layer B thickness on the optical properties of the proposed photonic structure. (a) Sensitivity variation, (b) shift in the PBG left edge, (c) shift in the PBG right edge, and (d) PBG width variation. The influence of gamma radiation exposure (0 and 70 Gy) on these parameters is also presented.

suggests that modifying the thickness of layer B can be an effective strategy for optimizing sensor performance, particularly in applications requiring precise refractive index detection.

PBG left edge *vs.* layer B thickness. The second graph shown in Fig. 8(b) presents the variation in the left edge of the PBG for different radiation doses. The results indicate that as layer B thickness increases, the left PBG edge shifts towards longer

wavelengths for both radiation doses. However, the shift is more pronounced under a higher radiation dose (70 Gy), highlighting the impact of radiation on the optical properties of the material.

After obtaining suitable thicknesses of layers A and B of the proposed dosimeter design further we have given our efforts to study the effect of changing the thickness of layer C of the structure on its PBG properties. For this purpose, we have calculated the left, right and width of the PBG along with the sensitivity of the structure dependent upon the thickness of layer C. All the data are summarized in Table 4.

Table 4 reveals how the thickness of layer C influences the PBG parameters and sensor sensitivity. As the thickness increases from 15 to 25 nm, the PBG left edge experiences a shift toward longer wavelengths while the right edge shifts toward shorter

T a b l e 4. Effect of layer C thickness on PBG characteristics, sensitivity, and intensity. The table presents variations in the left and right edges of the PBG, PBG width, PBG central wavelength, sensitivity, and average peak intensity as an increasing thickness of layer C, demonstrating its impact on the optical performance of the proposed sensor.

Layer C thickness [nm]	PBG left edge [nm]	PBG right edge [nm]	PBG width [nm]	Sensitivity [nm/RIU]	Average peak intensity [a.u.]	PBG center [nm]
15	529.35	669.95	140.6	181.0644	1	599.65
17.5	538.1	661.9	123.8	185.4733	0.999999	600
20	547.55	653.05	105.5	190.8508	0.999999	600.3
22.5	558.4	642.8	84.4	195.7206	0.999994	600.6
25	572.05	629.65	57.6	200.8351	0.999857	600.85

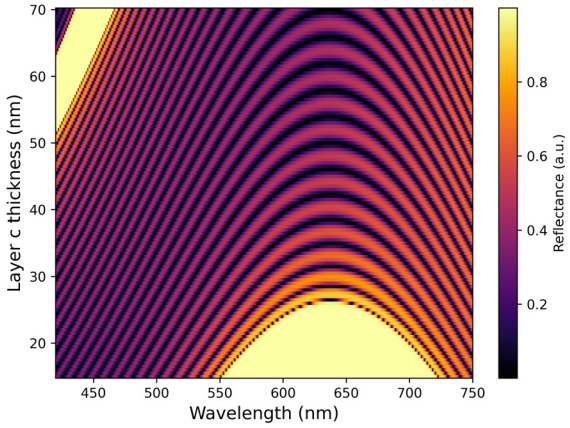

Fig. 9. Reflectance map showing the dependence of reflectance intensity on wavelength and layer C thickness. The color gradient represents reflectance values, with darker regions indicating lower reflectance and lighter regions representing higher reflectance. A distinct PBG region is observed, where light within a specific wavelength range is strongly reflected. The periodic interference pattern highlights the influence of layer thickness on optical properties, which is crucial for the design of optical coatings and sensor applications.

wavelengths, resulting in a narrowing of the PBG width from 140.6 down to 57.6 nm. Concurrently, sensitivity improves steadily, rising from 181.06 to 200.84 nm/RIU. The average peak intensity remains nearly constant, and the PBG center stabilizes around 600 nm. These trends suggest that increasing the thickness of layer C enhances the sen-

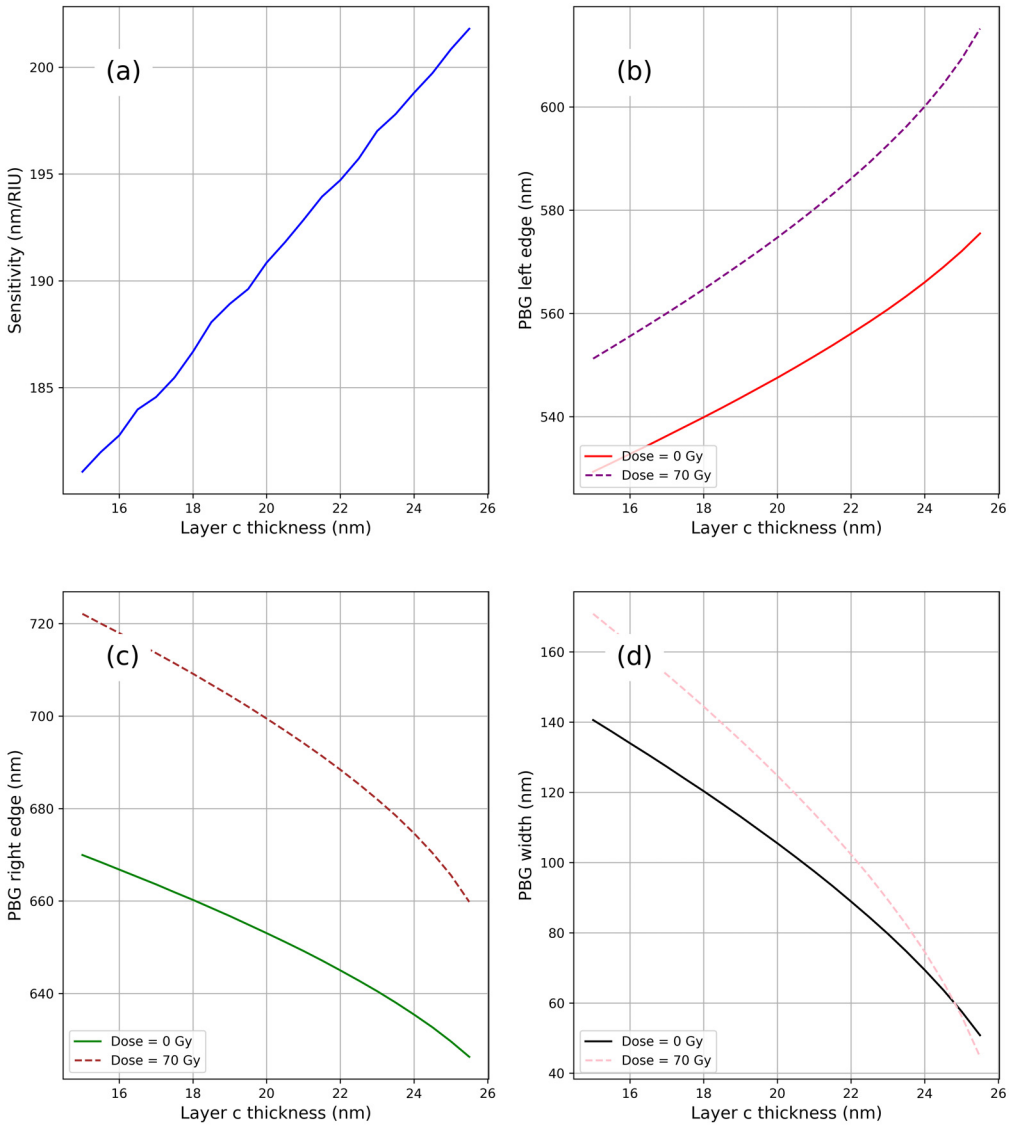

Fig. 10. Effect of layer C thickness on the optical properties of the proposed photonic structure. (a) Sensitivity variation, (b) shift in the PBG left edge, (c) shift in the PBG right edge, and (d) PBG width variation. The influence of gamma radiation exposure (0 and 70 Gy) on these parameters is also presented.

sor's ability to detect refractive index changes while fine-tuning the spectral properties of the photonic structure.

Figure 9 illustrates the variation of reflectance as a function of wavelength and the thickness of layer C, depicted through a color-mapped representation. The *x*-axis denotes the wavelength in nanometers, while the *y*-axis corresponds to the thickness of layer C in nanometers. The color bar on the right indicates the reflectance in arbitrary units, with brighter regions signifying higher reflectance and darker areas representing lower reflectance. The observed interference pattern arises due to the optical properties of the thin film, where alternating constructive and destructive interference effects lead to periodic variations in reflectance. A prominent high-reflectance region appears near 600 nm, which is indicative of enhanced optical response at specific thicknesses. Such visualizations are crucial for designing thin-film coatings and optimizing photonic device performance. Figure 10 summarizes all other performance parameters for layer C as done for layers A and B.

After all previous optimization steps and getting the optimum design, Fig. 11 illustrates the reflectance variation of the optimized sensor structure as a function of wavelength and γ-dose. A distinct PBG region is visible, which shifts with increasing radiation dose, indicating a modification in the optical properties of the structure. The gradual blue shift of the PBG with higher γ-dose suggests that radiation exposure alters the refractive index distribution, affecting the overall reflectance behavior. Additionally, the pattern of alternating high and low reflectance regions remains consistent across the spectrum, signifying the stability of the multilayer interference effect. The observed response demonstrates the sensor's potential for radiation dosimetry applications, as it exhibits a clear and measurable spectral shift in response to varying γ-dose levels.

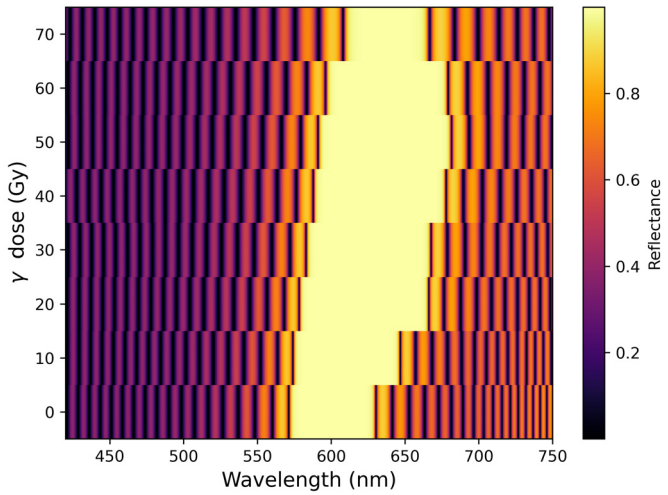

Fig. 11. Heatmap of the reflectance spectra of the optimized sensor structure as a function of γ-dose, showing a shift in the photonic bandgap with increasing radiation exposure.

5. Conclusion

In summary, the analysis of the optimized multilayer photonic structure highlights its effectiveness as a radiation sensor. The reflectance spectra indicate a clear photonic bandgap (PBG) that shifts in response to changes in the inner core radius and γ-dose, demonstrating sensitivity to both structural and environmental variations. The observed spectral shifts underscore the impact of radiation on the refractive index, making this design well-suited for dosimetry applications. Furthermore, the stability of the interference pattern under various conditions ensures reliable sensing performance. Optimizing the dosimeter involves determining the most effective thickness for each of the three layers, all aimed at enhancing the sensor's functionality. When these parameters are carefully adjusted, the sensor achieves a sensitivity of 200.8351 nm/RIU, enabling accurate detection of γ-ray radiation exposure ranging from 0 to 70 Gy. Overall, this study confirms that the proposed photonic structure can act as a precise and adjustable platform for radiation detection, with promising applications in both medical and industrial sectors.

Author contributions statement
Project administration, A. A. A., A. M., S. K. A., N. S. A., M. R. A., J. W., W. A. Z., and H. A. E.; Supervision, A. M., and H. A. E.; Software, A. A. A.; Visualization, A. A. A., A. M., and H. A. E.; Writing—review & editing; S. K. A., H. A. E., and A. M.; Writing—original draft, S. K. A.; Methodology, A. A. A., A. M., S. K. A., N. A. A., and H. A. E.; All authors have read and agreed to the published version of the manuscript.

Availability of data and material
The datasets used and/or analyzed during the current study available from the corresponding author on reasonable request.

Declarations
Conflict of interest The authors declare no conflict of interest.

Acknowledgment
This research was supported by Researchers Supporting Project number (RSPD2025R804), King Saud University, Riyadh, Saudi Arabia.

References

[1] Sheha E., Khoder H., Shanap T.S., El-Shaarawy M.G., El Mansy M.K., *Structure, dielectric and optical properties of p-type (PVA/CuI) nanocomposite polymer electrolyte for photovoltaic cells*, Optik **123**(13), 2012: 1161-1166. https://doi.org/10.1016/j.ijleo.2011.06.066

[2] Virtanen S., Vartianen J., Setala H., Tammelin T., Vuoti S., *Modified nanofibrillated cellulose -polyvinyl alcohol films with improved mechanical performance*, RSC Advances **4**(22), 2014: 11343 -11350. https://doi.org/10.1039/C3RA46287K

[3] Gad Y.H., Ali H.E., Hegazy E.S.A., *Radiation-induced improving mechanical and thermal properties of carboxymethyl cellulose/clay composite for application in removal of copper (II) ions from wastewater*, Journal of Inorganic and Organometallic Polymers and Materials **31**, 2021: 2083-2094. https://doi.org/10.1007/s10904-020-01850-w

[4] Pettignano A., Charlot A., Fleury E., *Solvent-free synthesis of amidated carboxymethyl cellulose derivatives: Effect on the thermal properties*, Polymers **11**(7), 2019: 1227. https://doi.org/10.3390/polym11071227

[5] Mazuki N.F., Abdul Majeed A.P.P., Nagao Y., Samsudin A.S., *Studies on ionics conduction properties of modification CMC-PVA based polymer blend electrolytes via impedance approach*, Polymer Testing **81**, 2020: 106234. https://doi.org/10.1016/j.polymertesting.2019.106234

[6] Suppiah K., Teh P.L., Husseinsyah S., Rahman R., *Properties and characterization of carboxymethyl cellulose/halloysite nanotube bio-nanocomposite films: Effect of sodium dodecyl sulfate*, Polymer Bulletin **76**, 2019: 365-386. https://doi.org/10.1007/s00289-018-2392-0

[7] Abou Taleb M.F., El-Mohdy H.L.A., El-Rehim H.A.A., *Radiation preparation of PVA/CMC copolymers and their application in removal of dyes*, Journal of Hazardous Materials **168**, 2009: 68-75. https://doi.org/10.1016/j.jhazmat.2009.02.001

[8] Rao V.N., Ravi P., Sathish M., Reddy N.L., Lee K., Sakar M., Prathap P., Kumari M.M., Reddy K.R., Nadagouda M.N., Aminabhavi T.M., Shankar M.V., *Monodispersed core/shell naNSnospheres of ZnS/NiO with enhanced H_2 generation and quantum efficiency at versatile photocatalytic conditions*, Journal of Hazardous Materials **413**, 2021: 125359. https://doi.org/10.1016/j.jhazmat.2021.125359

[9] El Sayed A.M., *Synthesis and controlling the optical and dielectric properties of CMC/PVA blend via γ-rays irradiation*, Nuclear Instruments and Methods in Physics Research Section B: Beam Interactions with Materials and Atoms **321**, 2014: 41-48. https://doi.org/10.1016/j.nimb.2013.12.020

[10] Zhao L., Mitomo H., Zhai M., Yoshii F., Nagasawa N., Kume T., *Synthesis of antibacterial PVA/CM-chitosan blend hydrogels with electron beam irradiation*, Carbohydrate Polymers **53**(4), 2003: 439-446. https://doi.org/10.1016/S0144-8617(03)00103-6

[11] Nouh S.A., Nagla A.G., Othman M.H., Eman S.A., Lotfi Z.I., *Thermal, structural, and optical properties of γ-irradiated poly(vinyl alcohol)/poly(ethylene glycol) thin film*, Journal of Applied Polymer Science **124**(1), 2012: 654-660. https://doi.org/10.1002/app.35010

[12] Nouh S.A., Radwan Y.E., Elfiky D., Abutalib M.M., Bahareth R.A., Hegazy T.M., Fouad S.S., *Structure, thermal, optical and electrical investigation of the effect of heavy highly energetic ions irradiations in Bayfol DPF 5023 nuclear track detector*, Radiation Physics and Chemistry **97**, 2014: 68-74. https://doi.org/10.1016/j.radphyschem.2013.10.017

[13] Yamauchi T., Nakai H., Somaki Y., Oda K., *Formation of CO_2 gas and OH groups in CR-39 plastics due to gamma-ray and ions irradiation*, Radiation Measurements **36**(1-6), 2003: 99-103. https://doi.org/10.1016/S1350-4487(03)00102-1

[14] Qiu J., Jiang X., Zhu C., Inouye H., Si J., Hirao K., *Optical properties of structurally modified glasses doped with gold ions*, Optics Letters **29**(4), 2004: 370-372. https://doi.org/10.1364/OL.29.000370

[15] Aly A.H., Elsayed H., *Defect mode properties in a one-dimensional photonic crystal*, Physica B: Condensed Matter **407**, 2012: 120-125. https://doi.org/10.1016/j.physb.2011.09.137

[16] Haberko J., Froufe-Pérez L.S., Scheffold F., *Transition from light diffusion to localization in three-dimensional amorphous dielectric networks near the band edge*, Nature Communications **11**, 2020: 4867. https://doi.org/10.1038/s41467-020-18571-w

[17] Yablonovitch E., Gmitter T.J., Leung K.M., *Photonic band structure: The face-centered-cubic case employing nonspherical atoms*, Physical Review Letters **67**(17), 1991: 2295-2298. https://doi.org/10.1103/PhysRevLett.67.2295

[18] McCall S.L., Platzman P.M., Dalichaouch R., Smith D., Schultz S., *Microwave propagation in two-dimensional dielectric lattices*, Physical Review Letters **67**(15), 1991: 2017-2020. https://doi.org/10.1103/PhysRevLett.67.2017

[19] Mehaney A., Elsayed H.A., Ahmed A.M., *Detection of isoprene traces in exhaled breath by using photonic crystals as a biomarker for chronic liver fibrosis disease*, 2021. https://doi.org/10.21203/rs.3.rs-443784/v1

[20] ABADLA M.M., ELSAYED H.A., MEHANEY A., *Thermo-optical properties of binary one dimensional annular photonic crystal including temperature dependent constituents*, Physica E: Low-dimensional Systems and Nanostructures **119**, 2020: 114020. https://doi.org/10.1016/j.physe.2020.114020

[21] ELSAYED H.A., MEHANEY A., *Theoretical verification of photonic crystals sensor for biodiesel detection and sensing*, Physica Scripta **95**(8), 2020: 085507. https://doi.org/10.1088/1402-4896/aba2b1

[22] AHMED A.M., MEHANEY A., *Ultra-high sensitive 1D porous silicon photonic crystal sensor based on the coupling of Tamm/Fano resonances in the mid-infrared region*, Scientific Reports **9**, 2019: 6973. https://doi.org/10.1038/s41598-019-43440-y

[23] CHIAPPINI A., TRAN L.T.N., TREJO-GARCÍA P.M., ZUR L., LUKOWIAK A., FERRARI M., RIGHINI G.C., *Photonic crystal stimuli-responsive chromatic sensors: A short review*, Micromachines **11**(3), 2020: 290. https://doi.org/10.3390/mi11030290

[24] BACCINI D., HINCKLEY S., CANNING J., COOK K., ALLWOOD G., WILD G., DAVIES J., BANOS C., *Gamma irradiation response in photonic crystal and standard optical fiber Bragg grating sensors for radiation dosimetry*, Proceedings of the SPIE, Vol. 11200, AOS Australian Conference on Optical Fiber Technology (ACOFT) and Australian Conference on Optics, Lasers, and Spectroscopy (ACOLS) 2019, International Society for Optics and Photonics, 2019: 112000O. https://doi.org/10.1117/12.2539904

[25] YUE X., LI H., LV X., TANG J., *Porous silicon photonic crystal/silver composite produced by microwave-assisted reduction: Applications to surface-enhanced Raman scattering*, Optical Materials: X, **2**, 2019: 100027. https://doi.org/10.1016/j.omx.2019.100027

[26] DAHER M.G., JAROSZEWICZ Z., ZYOUD S.H., PANDA A., AHAMMAD S.H., ABD-ELNABY M., EID M.M.A., RASHED A.N.Z., *Design of a novel detector based on photonic crystal nanostructure for ultra high performance detection of cells with diabetes*, Optical and Quantum Electronics **54**, 2022: 701. https://doi.org/10.1007/s11082-022-04093-w

[27] DAHER M.G., TRABELSI Y., PANDA A., GEVORGYAN A.H., ABOHASSAN K.M., SMIRANI L.K., ALTAHAN B.R., RASHED A.N.Z., *Design of a highly sensitive detector using a ternary photonic crystal (PC) based on titanium nitride sandwiched between Si and SiO_2 for the creatinine concentration detection in the blood serum*, Optics **3**(4), 2022: 447-461. https://doi.org/10.3390/opt3040038

[28] DAHER M.G., *Supersensitive biosensor based on a photonic crystal nanostructure for blood sugar level monitoring with ultra-high quality factor and low detection limit*, Optik **275**, 2023: 170581. https://doi.org/10.1016/j.ijleo.2023.170581

[29] DAHER M.G., ALSALMAN O., AHMED N.M., SASSI I., SORATHIYA V., HEI CHIT LEO TSUI, PATEL S.K., *Modeling of a novel chikungunya virus detector based on silicon and titanium nitride multilayer thin films*, Optik **287**, 2023: 171136. https://doi.org/10.1016/j.ijleo.2023.171136

[30] ZAKY Z.A., SHARMA A., ALY A.H., *Tamm plasmon polariton as refractive index sensor excited by gyroid metals/porous Ta_2O_5 photonic crystal*, Plasmonics **17**(2), 2022: 681-691. https://doi.org/10.1007/s11468-021-01559-7

[31] ZHONG F., MO J., LI Y., SUN B., WU Z., *Optical characteristics of porous silicon photonic crystals prepared on the back surface of silicon wafers*, Optik **201**, 2020: 163486. https://doi.org/10.1016/j.ijleo.2019.163486

[32] ALY A.H., RYU S.-W., HSU H.-T., WU C.-J., *THz transmittance in one-dimensional superconducting nanomaterial-dielectric superlattice*, Materials Chemistry and Physics **113**(1), 2009: 382-384. https://doi.org/10.1016/j.matchemphys.2008.07.123

[33] EL-SHEMY S., ALY A.H., SAYED H., EISSA M.F., *Production of intensifying blue light by Cherenkov radiation phenomena and its application as a power source*, Optical and Quantum Electronics **54**, 2022: 70. https://doi.org/10.1007/s11082-021-03444-3

[34] ENTEZAM A., KHANDAKER M.U., AMIN Y.M., UNG N.M., BRADLEY D.A., MAAH J., SAFARI M.J., MORADI F., *Thermoluminescence response of Ge-doped cylindrical-, flat- and photonic crystal silica-fibres to electron and photon radiation*, PLoS ONE **11**(5), 2016: e0153913. https://doi.org/10.1371/journal.pone.0153913

[35] Nouh S.A., Benthami K.A., AlSomali F., Yajzey R., Bakeer D.E.S., *Impact of gamma radiation on the linear and nonlinear optical properties of PVA/CMC/ZnS-NiO nanocomposite films*, Radiation Effects and Defects in Solids **179**(1-2), 2024: 43-63. https://doi.org/10.1080/10420150.2024.2318710

[36] Zhong K., Liu L., Xu X., Hillen M., Yamada A., Zhou X., Verellen N., Song K., Van Cleuvenbergen S., Vallée R., Clays K., *Defect mode passband lasing in self-assembled photonic crystal*, ACS Photonics **3**(12), 2016: 2330-2337. https://doi.org/10.1021/acsphotonics.6b00511

[37] Kennedy S.R., Brett M.J., Toader O., John S., *Fabrication of tetragonal square spiral photonic crystals*, Nano Letters **2**(1), 2002: 59-62. https://doi.org/10.1021/nl015635q

[38] Sabra W., Elsayed H.A., Mehaney A., Aly A.H., *Numerical optimization of 1D superconductor photonic crystals pressure sensor for low temperatures applications*, Solid State Communications **343**, 2022: 114671. https://doi.org/10.1016/j.ssc.2022.114671

[39] Gandhi S., Awasthi S.K., *Analysis and detection of women's reproductive hormones using a bistable and reconfigurable 1D annular photonic crystal composed of the $Ge_2Sb_2Te_5$ phase-change material*, RSC Advances **12**(47), 2022: 30335-30348. https://doi.org/10.1039/D2RA04238J

[40] Gandhi S., Awasthi S.K., Aly A.H., *Biophotonic sensor design using a 1D defective annular photonic crystal for the detection of creatinine concentration in blood serum*, RSC Advances **11**(43), 2021: 26655-26665. https://doi.org/10.1039/D1RA04166E

[41] Gandhi S., Awasthi S.K., *Protein detection capabilities of photonic biosensor composed of 1D annular photonic crystal*, Results in Optics **15**, 2024: 100639. https://doi.org/10.1016/j.rio.2024.100639

[42] Gandhi S., Awasthi S.K., *Biophotonic sensor design for the detection of reproductive hormones in females by using a 1D defective annular photonic crystal*, International Journal of Materials Research **114**(7-8), 2023: 618-627. https://doi.org/10.1515/ijmr-2021-8743

[43] Caruso R.A., Susha A., Caruso F., *Multilayered titania, silica, and laponite nanoparticle coatings on polystyrene colloidal templates and resulting inorganic hollow spheres*, Chemistry of Materials **13**(2), 2001: 400-409. https://doi.org/10.1021/cm001175a

[44] Caroselli R., Martín Sánchez D., Ponce Alcántara S., Prats Quilez F., Torrijos Morán L., García-Rupérez J., *Real-time and in-flow sensing using a high sensitivity porous silicon microcavity-based sensor*, Sensors **17**(12), 2017: 2813. https://doi.org/10.3390/s17122813

[45] Ibrahim M.S.S., Hamed M.K.G., El-Okr M.M., Obayya S.S.A., Hameed M.F.O., *Highly sensitive photonic crystal gamma ray dosimeter*, Optical and Quantum Electronics **53**, 2021: 348. https://doi.org/10.1007/s11082-021-02968-y

[46] Sayed F.A., Elsayed H.A., Mehaney A., Eissa M.F., Aly A.H., *A doped-polymer based porous silicon photonic crystal sensor for the detection of gamma-ray radiation*, RSC Advances **13**(), 2023: 3123-3138. https://doi.org/10.1039/D2RA07637C

[47] Zaky Z.A., Al-Dossari M., Hendy A.S., Zayed M., Aly A.H., *Gamma radiation detector using Cantor quasi-periodic photonic crystal based on porous silicon doped with polymer*, International Journal of Modern Physics B **38**(30), 2024: 2450409. https://doi.org/10.1142/S0217979224504095

[48] El-Shemy S., Semeda R., Mobarak M., Eissa M.F., Sayed F.A., Alshomrany A.S., Aly A.H., *Radiation sensor based on a 1D-periodic structure infiltrated by (B-co-MP) a conjugated copolymer*, Scientific Reports **14**, 2024: 19829. https://doi.org/10.1038/s41598-024-65312-w

Received March 21, 2025
in revised form April 17, 2025